inorganics

MDPI

Article

A Theoretical Comparison on Pd-Doped $MoSe_2$, WSe_2, and $MoSe_2$-WSe_2 for Adsorption and Sensing of Dissolved Gases (H_2, C_2H_2, and C_2H_4) in Transformer Oil

Xinyu Guo [1], Shouxiao Ma [1] and Hao Cui [2,*]

[1] CHN Energy Qinghai Electric Power Co., Ltd., Xining 810001, China
[2] College of Artificial Intelligence, Southwest University, Chongqing 400715, China
* Correspondence: cuihaocqu@163.com

Abstract

This study presents a comprehensive first-principles investigation into the gas adsorption and sensing characteristics of Pd-doped $MoSe_2$, WSe_2, and $MoSe_2$-WSe_2 systems for dissolved gas analysis applications in oil-filled transformers. Through theoretical simulations, we first establish and characterize three distinct Pd-doped systems, examining their structural stability, electronic properties, and gas interaction mechanisms with key typical gases (H_2, C_2H_2, and C_2H_4). Our analysis reveals that the Pd@$MoSe_2$-WSe_2 heterojunction exhibits exceptional sensing performance, with calculated response values of −77.67% (H_2), −95.98% (C_2H_2), and −96.88% (C_2H_4)—significantly surpassing the capabilities of both Pd-$MoSe_2$ and Pd-WSe_2 monolayers. The observed response hierarchy (C_2H_4 > C_2H_2 > H_2) correlates directly with the degree of adsorption energy, charge transfer, and bandgap modification induced by gas adsorption. Finally, the reason for such enhancements are systemically analyzed. The findings not only position Pd@$MoSe_2$-WSe_2 as an outstanding candidate for condition evaluation in oil-filled transformers but also establish a structure–property relationship that uncovers the feasibility of a strategic heterojunction design to enhance the adsorption and sensing performances for typical gas species.

Keywords: Pd@$MoSe_2$-WSe_2; first-principles theory; oil-filled transformers; gas sensor

check for updates

Academic Editor: Jean Pierre Djukic

Received: 28 September 2025
Revised: 19 October 2025
Accepted: 24 October 2025
Published: 28 October 2025

Citation: Guo, X.; Ma, S.; Cui, H. A Theoretical Comparison on Pd-Doped $MoSe_2$, WSe_2, and $MoSe_2$-WSe_2 for Adsorption and Sensing of Dissolved Gases (H_2, C_2H_2, and C_2H_4) in Transformer Oil. *Inorganics* **2025**, *13*, 360. https://doi.org/10.3390/inorganics13110360

Copyright: © 2025 by the authors. Licensee MDPI, Basel, Switzerland. This article is an open access article distributed under the terms and conditions of the Creative Commons Attribution (CC BY) license (https://creativecommons.org/licenses/by/4.0/).

1. Introduction

In urban power distribution networks, oil-filled transformers serve as critical components for efficient electricity transmission and reliable power system operation [1,2]. These transformers utilize mineral oil as an insulating medium, whose integrity can be compromised by partial discharges and other insulation degradation mechanisms [3,4]. Over prolonged operation, such electrical discharges induce the decomposition of insulating oil, generating various gaseous byproducts—predominantly H_2, C_2H_2, and C_2H_4—which dissolve in the oil and may form gas bubbles [5,6]. Extensive research has demonstrated that these dissolved gases progressively deteriorate the dielectric properties of the insulating oil, potentially compromising transformer performance and operational safety [7,8]. To monitor the operational health of oil-filled transformers, dissolved gas analysis (DGA) has been established as a standard diagnostic technique [9]. This methodology involves the extraction and quantitative analysis of dissolved gases from transformer oil using sensitive detection systems. Through the precise identification and quantification of these gaseous components, DGA enables the detection of incipient insulation faults and assessment of

their severity [10]. Over decades of development, DGA has evolved into a robust and reliable approach for transformer condition monitoring [11]. The efficacy of this technique fundamentally depends on the availability of highly sensitive gas detection methods capable of accurately measuring trace concentrations of key gas species in transformer oil [12]. Such capabilities are essential for comprehensive condition assessment, thereby ensuring the continued reliability and safety of power distribution infrastructure.

In the pursuit of advanced gas detection solutions, nanomaterial-based sensors have emerged as a promising alternative to conventional gas spectrum technology, offering distinct advantages in operational simplicity, cost-effectiveness, compact form factors, and superior sensitivity [13,14]. This has driven remarkable progress in nano-sensor technology development in recent years, with particular emphasis on two-dimensional (2D) material systems [15–18]. Among these, transition metal dichalcogenides (TMDs) have attracted considerable research interest due to their theoretically predicted and experimentally validated exceptional sensitivity and rapid response characteristics in gas sensing applications [19–21]. Representative compounds such as MoX_2 and WX_2 (where X = S, Se, or Te) have been extensively investigated for their gas detection capabilities across various target species [22–25]. These materials demonstrate superior sensing performance metrics, thereby creating new research opportunities in the field of gas sensor development [26,27].

Very recently, TMD-based heterostructures have increasingly been explored and successfully synthesized for gas sensing applications [28,29]. For instance, Muhammad Ikram et al. fabricated an MoS_2/WS_2 heterojunction and proved its favorable room-temperature NO_2 sensing properties [30]. Similarly, Priyakshi Kalita et al. synthesized an $MoSe_2$-WSe_2 heterojunction and reported that the hybrid material exhibited an excellent H_2 sensing performance, along with strong humidity tolerance and stability [31]. Beyond experimental synthesis, theoretical calculations have been employed to predict the geometric and electronic properties of such heterojunctions. For example, Fabrizio Creazzo's group investigated key interfacial properties—including electronic structure, water organization, surface electric field, and work function—of the $MoSe_2$-WSe_2 heterojunction using molecular dynamics simulations [32]. These studies highlight the favorable gas sensing property of the $MoSe_2$-WSe_2 heterojunction. Therefore, it is assumed that the theoretical simulations of gas adsorption on $MoSe_2$-WSe_2 heterostructure would provide valuable insights to elucidate the gas sensing mechanisms of TMDs heterostructures.

Beyond heterojunctions, there have been numerous studies illustrating the efficacy of modifying nanomaterial surfaces with metal atoms to enhance gas adsorption and sensing performance [33,34]. However, few studies have systematically investigated the effects of this surface modification strategy on heterojunctions for gas sensing applications. To bridge this knowledge gap, we employ first-principles calculations to elucidate the gas sensing mechanisms of the metal-doped $MoSe_2$-WSe_2 heterojunction. Specifically, we selected Pd as the dopant in this work due to its well-established catalytic properties in gas–molecule interactions [35,36]. In other words, we propose a Pd-doped $MoSe_2$-WSe_2 heterojunction (denoted as Pd@$MoSe_2$-WSe_2) in this work as a novel sensing candidate to conduct DGA for oil-filled transformers. Three dominant gas species under early-stage insulation defects, including H_2, C_2H_2, and C_2H_4, are selected as the targeted gases to evaluate the sensing performance of our proposed materials. Such selection can ensure the in-time evaluation of insulation defects in oil-filled transformers. On the other hand, the saturated gases such as CH_4 are excluded in this study, which have been consistently reported in the previous literature to exhibit minimal reactivity and weak adsorption interactions with Pd-doped surfaces [21]. By establishing a structure–property relationship in metal-doped TMD heterojunctions, this research contributes to the ongoing development of advanced gas sensing technologies. Furthermore, to give a deeper evaluation on the sensing performance,

we conduct comparative analyses between the Pd@$MoSe_2$-WSe_2 heterojunction and the Pd-doped $MoSe_2$ and Pd-WSe_2 (Pd-$MoSe_2$ and Pd-WSe_2) monolayers to uncover the critical impact of interfacial effects on the gas sensing properties. The insights gained from this work can not only reveal the atomic-level gas adsorption mechanisms on metal-doped TMD heterojunctions but also expand the potential applications of heterojunction-based materials for advanced gas sensor development, particularly in the field of DGA for oil-filled transformers.

2. Computational Details

The first-principles simulations were performed using the DMol^3 module [37], employing the Perdew–Burke–Ernzerhof (PBE) functional to account for exchange-correlation effects in both geometric optimization and electronic structure calculations [38]. To accurately describe van der Waals interactions and long-range effects, we incorporated dispersion corrections through the Tkatchenko–Scheffler (TS) scheme within the DFT-D3 framework [39]. In terms of Billouin-zone integration, a Monkhorst–Pack *k*-point grid of $10 \times 10 \times 1$ was adopted for all geometric optimizations and electronic property calculations [40]. The convergence criteria for geometry optimization were set at an energy threshold of 10^{-5} Ha, with a global orbital cutoff radius of 5.0 Å, specifically chosen to properly describe the metal atoms' electronic states [41]. The electronic structure was represented using a double numerical plus polarization (DNP) basis set for all atomic orbitals in our calculations without considering the basis set superposition errors (BSSE) as their negligible influence on the system's total energy [42].

The $MoSe_2$-WSe_2 heterojunction was constructed by first modeling $4 \times 2 \times 1$ supercells of individual $MoSe_2$ and WSe_2 monolayers, followed by the formation of a seamless lateral interface between two monolayers within the same plane. These initial structures of $MoSe_2$ and WSe_2 monolayers were built atom-by-atom using the visualization and modeling software, Materials Studio 2020. Then, two interfaces were designed with Se-terminated edges to ensure optimal bonding configuration. Subsequently, the Pd@$MoSe_2$-WSe_2 system was created via surface modification, wherein a single Pd atom was adsorbed onto the heterojunction surface, followed by geometric optimization of the composite structure. Such modification corresponds to a calculated Pd-doping concentration of 2.08%. To eliminate potential interactions between adjacent units during gas adsorption, a vacuum region of 20 Å was introduced along the *z*-axis of the heterojunction system [43]. For electronic structure analysis, we employed Hirshfeld population analysis to quantify the charge of Pd adatom (Q_{Pd}) in the Pd@MoS_2-WSe_2 system and the charge transfer (Q_T, the charge of adsorbed gas species) in the gas-adsorbed systems. Based on this definition, positive values indicated the electron-donating property of the analytes, while negative values reflected electron-accepting behavior. These systematic approaches enable comprehensive characterization of both the structural and electronic properties of the modified heterojunction system for gas sensing applications.

3. Results and Discussion

3.1. Analysis of Isolated and Pd-Doped $MoSe_2$-WSe_2 Configuration

The construction process of the $MoSe_2$-WSe_2 heterojunction is illustrated in Figure 1. Since this heterojunction requires the formation of a seamless lateral interface between $MoSe_2$ and WSe_2 monolayers within the same plane, we first analyzed the structural parameters of the pristine monolayers. Our calculations reveal that the optimized lattice constants are 3.30 Å for $MoSe_2$ and 3.34 Å for WSe_2, as exhibited in Figure 1a,b, with corresponding metal–chalcogen bond lengths of 2.55 Å (Mo-Se) and 2.56 Å (W-Se). These results show favorable agreement with the reported values for these monolayers [44,45]. The marginally larger lattice

constant and bond length in WSe_2 can be attributed to the greater covalent radius of W (1.62 Å) compared to Mo (1.54 Å) [46]. Importantly, the minimal lattice mismatch (<1.2%) between two monolayers demonstrates their exceptional compatibility for forming in-plane heterojunctions with good structural integrity in the composite system [47].

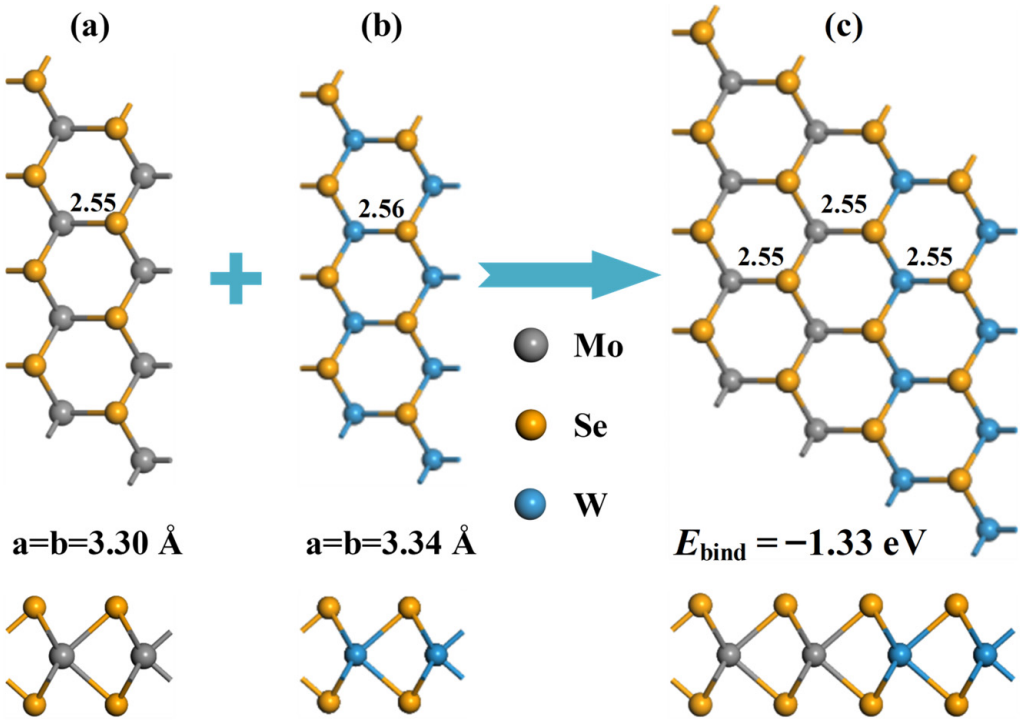


Figure 1. Construction process of the $MoSe_2$-WSe_2 heterojunction. (**a**) $MoSe_2$, (**b**) WSe_2, and (**c**) $MoSe_2$-WSe_2 heterojunctions.

Upon the optimized $MoSe_2$-WSe_2 heterojunction shown in Figure 1c, it is revealed that the Mo-Se and W-Se bond lengths maintain a consistent value of 2.55 Å across the $MoSe_2$ domain, WSe_2 domain, and the heterojunction interface. This indicates a slight geometric activation of the WSe_2 component during heterojunction formation, a minor contraction of W-Se bonds from 2.56 Å that enhances the structural compactness with negligible interfacial strain and favorable structural stability [48]. To further evaluate the interfacial stability of the optimized $MoSe_2$-WSe_2 heterojunction, we calculated the binding energy (E_{bind}) using [49]

$$E_{bind} = E_{MoSe_2-WSe_2} - \frac{1}{2}E_{MoSe_2} - \frac{1}{2}E_{WSe_2} \quad (1)$$

where $E_{MoSe_2-WSe_2}$ indicates the total energy of the heterojunction system, while E_{MoSe_2} and E_{WSe_2} donate the total energies of the pristine WS_2 and WSe_2 in the $4 \times 4 \times 1$ lattice, respectively.

According to our calculations, the E_{bind}, normalized per unit cell of the heterojunction, is −1.33 eV, which reveals the strong interfacial coupling between the constituent monolayers and the thermodynamic favorability for the formation of the heterojunction [50]. The structural integrity of the heterojunction is essential for its performance as a stable nano-substrate in gas sensing applications, serving as an effective candidate for subsequent surface modifications and gas adsorption studies.

Then, the adsorption process of a Pd atom onto the $4 \times 4 \times 1$ supercells of $MoSe_2$, WSe_2, and $MoSe_2$-WSe_2 are carried out to construct the Pd-$MoSe_2$, Pd-WSe_2, as well as Pd@$MoSe_2$-WSe_2 configurations, as exhibited in Figure 2. For the heterojunction system, six distinct adsorption sites are considered, as shown in Figure 2(a1), traced as the T_{Mo1}

site (on the top of the Mo atom of the $MoSe_2$ side), $H_{Mo\text{-}Se}$ site (on the top of the hollow Mo-Se ring), T_{Mo2} site (on the top of the Mo atom of the heterojunction), $H_{Mo\text{-}W\text{-}Se}$ site (on the top of the hollow Mo-W-Se ring), T_W site (on the top of the W atom of the WS_2 side), and $H_{W\text{-}S}$ site (on the top of the hollow W-S ring). In the case of Pd-doping in the $MoSe_2$, three adsorption sites are examined in Figure 2(b1), traced as the T_{Se} site (on the top of the Se atom), $H_{Mo\text{-}Se}$ site (on the top of the hollow Mo-Se ring), and T_{Mo} site (on the top of the Mo atom). Similarly, Figure 2(c1) shows the analogous adsorption sites for the WSe_2, traced as the T_{Se} site (on the top of the Se atom), $H_{W\text{-}Se}$ site (on the top of the hollow W-Se ring), and T_W site (on the top of the W atom).

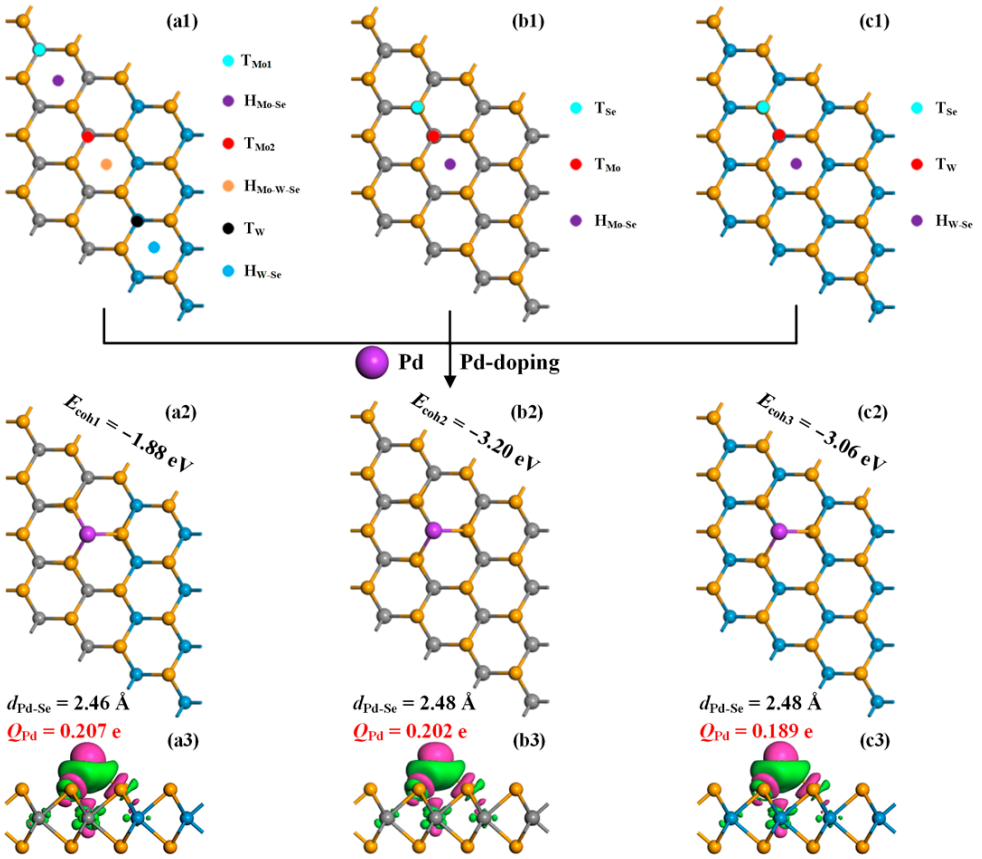


Figure 2. Pd-doping process including the preferred configuration and CDD of (**a1**–**a3**) $MoSe_2$-WSe_2, (**b1**–**b3**) $MoSe_2$, and (**c1**–**c3**) WSe_2. In CDD, the isosurface is set to 0.01 e/Å^3, and the green areas are electron accumulation, while the violet areas are electron depletion.

Following geometric optimization, the preferred configurations of three Pd-doped structures are displayed in Figure 2(a2–c2) with their related charge density differences (CDD) shown in Figure 2(a3–c3). These configurations are determined by the most negative cohesive energy (E_{coh}) among various adsorption sites, in which E_{coh1} for Pd@$MoSe_2$-WSe_2, E_{coh2} for Pd-$MoSe_2$, and E_{coh3} for Pd-WSe_2 are calculated as follows [51]:

$$E_{coh1} = E_{Pd@MoSe_2-WSe_2} - E_{MoSe_2-WSe_2} - E_{Pd} \quad (2)$$

$$E_{coh2} = E_{Pd-MoSe_2} - E_{MoSe_2} - E_{Pd} \quad (3)$$

$$E_{coh3} = E_{Pd-WSe_2} - E_{WSe_2} - E_{Pd} \quad (4)$$

where $E_{Pd@MoSe_2-WSe_2}$, $E_{Pd-MoSe_2}$, and E_{Pd-WSe_2} indicate the total energy of the Pd-doped heterojunction, $MoSe_2$, and WSe_2 systems, respectively, and E_{Pd} indicates the energy of the single Pd atom in its bulk structure.

Analysis of the cohesive energies reveals a distinct Pd-doping performance in three monolayers. As plotted in Figure 2(a2), the preferred doping configuration in the $MoSe_2$-WSe_2 heterojunction is through the T_{Mo2} site, with an E_{coh1} of −1.88 eV. This value is considerably less negative than those on the other pristine monolayers: −3.20 eV at the T_{Mo1} site of $MoSe_2$ in Figure 2(b2) and −3.06 eV at the T_W site of WSe_2 in Figure 2(b3). The elevated E_{coh1} in the heterojunction can be primarily attributed to the unique electronic environment at the heterointerface. The built-in electric field and the lattice mismatch-induced strain collectively reduce the charge transfer efficiency and weaken the binding strength between Pd and the substrate. Despite this moderated binding, all three cohesive energies are significantly negative, unequivocally confirming the thermodynamic stability of the Pd adatom on each structure. Analysis of the geometric structures show that the Pd-Se bond length in the Pd@$MoSe_2$-WSe_2 heterojunction is 2.46 Å, marginally shorter than the value of 2.48 Å in the pristine Pd-$MoSe_2$ and Pd-WSe_2 systems. This difference stems from the altered local bonding environment at the heterointerface, where the mismatch between the $MoSe_2$ and WSe_2 layers modifies the optimal bonding geometry [52]. Furthermore, the vibrational frequency analysis is analyzed to verify the thermodynamic stability of three Pd-doped configurations, with characteristic modes spanning 68.50–779.22 cm^{-1} for Pd@$MoSe_2$-WSe_2, 70.37–801.80 cm^{-1} for Pd-$MoSe_2$, and 68.76–687.88 cm^{-1} for Pd-WSe_2, respectively. The absence of imaginary frequencies in these spectra provides definitive evidence that the structures are local minima on the potential energy surfaces.

The CDD analysis, as shown in Figure 2(a3–c3), reveals pronounced electron accumulation at the newly formed Pd-Se bonds accompanied by electron depletion around the Pd adatoms, which demonstrates strong covalent bonding characteristics and significant electron donation from the Pd sites. This electronic redistribution is quantitatively confirmed by the Hirshfeld charge analysis, which shows charges of +0.207, +0.202, and +0.189 e on the Pd dopants in Pd@$MoSe_2$-WSe_2, Pd-$MoSe_2$, and Pd-WSe_2 systems, respectively. The charge transfer originates from the electronegativity difference between Se (2.55) and Pd (2.20), driving electron donation from Pd to the surrounding Se atoms during bond formations [53]. These results manifest that, while all configurations exhibit stable bonding, the heterojunction shows a slightly enhanced binding force and charge transfer in comparison to the pristine monolayers, suggesting more superior stability for typical applications.

To elucidate the influence of Pd-doping on the electronic properties of $MoSe_2$, WSe_2, and $MoSe_2$-WSe_2 systems, we performed a comparative analysis of band structures (BS) and the density of states (DOS) for both pristine and Pd-doped configurations, as presented in Figure 3. Notably, the symmetric spin-up and spin-down states observed in all systems reveal their non-magnetic nature, which remains unchanged regardless of Pd-doping. The BS calculations demonstrate that pristine $MoSe_2$ and WSe_2 monolayers exhibit characteristic direct bandgaps of 1.546 eV and 1.523 eV, as shown in Figure 3(a1,b1). The formation of the $MoSe_2$-WSe_2 heterojunction preserves this direct bandgap nature while inducing a modest reduction to 1.440 eV, as seen in Figure 3(c1). This bandgap narrowing may be attributed to the interfacial interactions and orbital hybridization at the junction boundary that facilitates the charge carrier transport, which is consistent with the established reports on TMDs-based in-plane heterojunctions [54]. Moreover, the introduction of Pd dopants further modifies the electronic structure, as evidenced by the reduced bandgaps of 1.422 eV for Pd-$MoSe_2$, 1.464 eV for Pd-WSe_2, and 1.398 eV for Pd@$MoSe_2$-WSe_2 in Figure 3(a2–c2). These reductions result from the formation of impurity states within the original bandgap, as observed in the DOS distributions in Figure 3(a3–c3), where significant Pd-derived states appear near the Fermi level [55]. While these additional states enhance electron mobility through improved carrier transport, they do not alter the direct semiconductor character of any system, confirming the electronic stability of both the isolated and Pd-

doped configurations. Furthermore, the orbital DOS analysis elucidates the chemical bonding nature in Pd-doped systems, revealing significant electron hybridization between the Pd 4*d* orbitals and Se 4*p* orbitals across all three configurations. This pronounced orbital interaction not only confirms the formation of stable Pd-Se covalent bonds but also substantiates the thermodynamic favorability of Pd-doping in both the monolayer and heterojunction systems. Of note is the electronic states the in Pd@$MoSe_2$-WSe_2 system, in which the Se1 atom at the $MoSe_2$ side reveals nearly equivalent contributions with the Se2 atom at the WSe_2 side in the hybridization with the Pd 4*d* orbitals, highlighting the structural integrity and electronic homogeneity of the modified system.

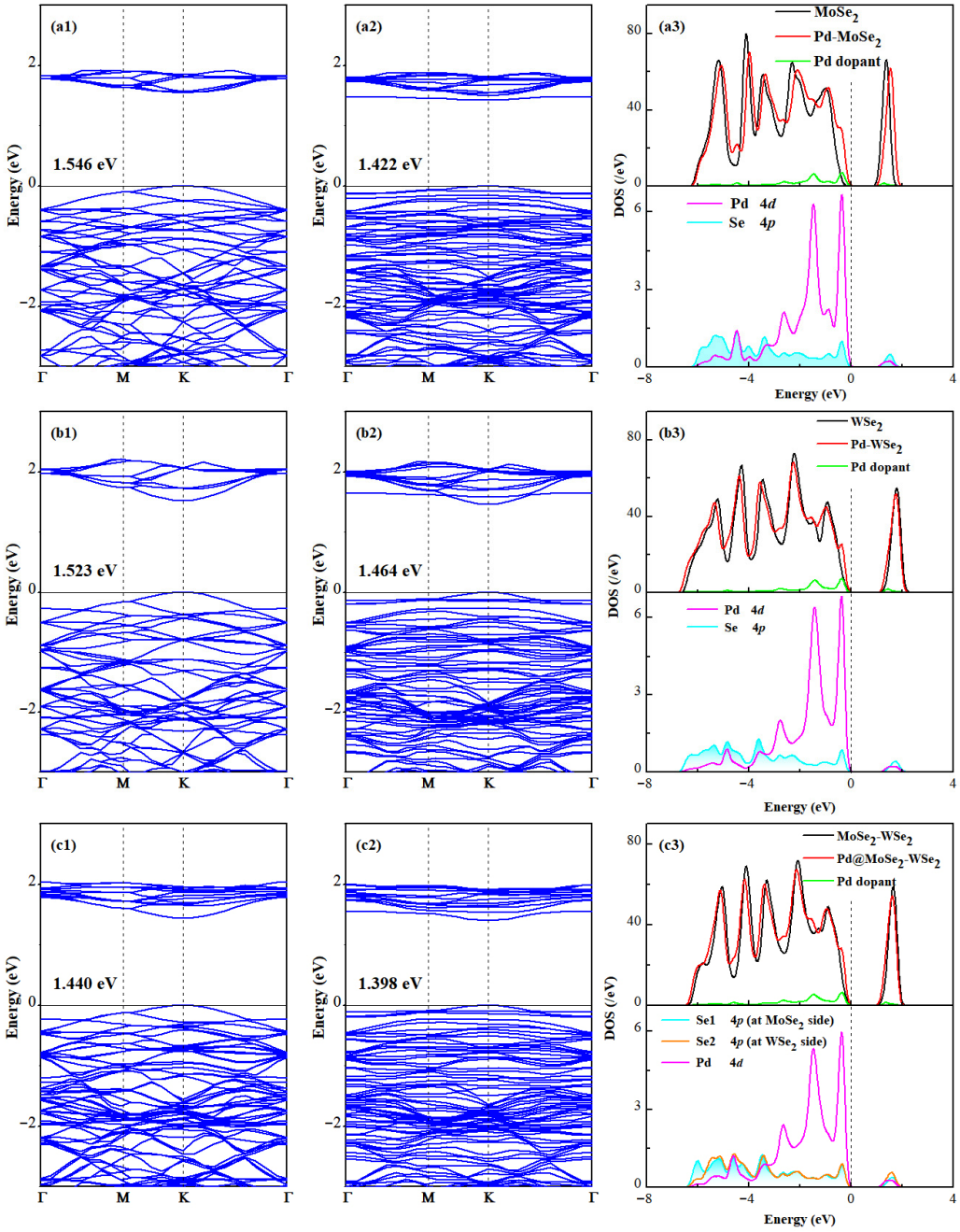


Figure 3. Electronic structures of isolated and Pd-doped $MoSe_2$, WSe_2, and $MoSe_2$-WSe_2 systems. (**a1**–**c1**) BS of isolated systems, (**a2**–**c2**) BS of Pd-doped systems, and (**a3**–**c3**) DOS of Pd-doped systems. In BS, the black values are the bandgaps, and in DOS, the dashed line is the Fermi level.

3.2. Gas Adsorptions on Pd-Doped $MoSe_2$, WSe_2, and $MoSe_2$-WSe_2

This section focuses on the adsorption performance of three Pd-doped systems (Pd@$MoSe_2$-WSe_2, Pd-$MoSe_2$, and Pd-WSe_2) upon three typical gas molecules (H_2, C_2H_2, and C_2H_4), with particular emphasis on the performance of the Pd-doped heterojunction system followed by comparison with the other Pd-doped systems. The adsorption configurations are generated by manually positioning gas molecules within the lattice framework of each Pd-doped system at an initial distance of about 2.5 Å from the Pd adatom. Such a distance is a critical distance that lies within the transition region between physisorption and chemisorption, as it approaches the characteristic range of van der Waals interactions between the gas molecules and adsorption surfaces [56]. With initial placement, geometric optimizations are performed to determine the most stable configuration (MSC) for each gas–surface combination, with the most negative adsorption energy (E_{ad}) calculated serving as the key thermodynamic parameter for the identification of MSC. This approach can also be applied to compare the adsorption performance across three nano-surfaces with consistent evaluation criteria for all gas–surface systems. The equation to calculate E_{ad} is

$$E_{ad} = E_{surface/gas} - E_{surface} - E_{gas} \quad (5)$$

wherein $E_{surface/gas}$ indicates the total energies of the gas-adsorbed Pd-doped surface, $E_{surface}$ indicates the total energies of the isolated Pd-doped surface, and E_{gas} is the total energies of the isolated gas molecule.

We first focus on the adsorption performance of the Pd@$MoSe_2$-WSe_2 heterojunction, with Figure 4 exhibiting the MSC and corresponding CDD plots for H_2, C_2H_2, and C_2H_4 adsorption. The analysis reveals that all three gas molecules undergo significant structural modifications upon adsorption associated with the formation of distinct chemical bonds with the Pd adatom. Typically, the Pd dopant forms two Pd-H bonds (1.81 Å) with H_2, while establishing two Pd-C bonds with both C_2H_2 (2.13 Å) and C_2H_4 (2.21 Å). These findings indicate the strong gas–surface interactions across these systems that lead to remarkable deformation in the gas molecules [57]. Specifically, the H-H bond elongates from 0.75 Å in the free molecule to 0.82 Å upon adsorption, while C_2H_2 loses its linear geometry, and C_2H_4 deviates from planarity. These structural alterations, combined with the calculated E_{ad} of −0.31 eV (H_2), −0.93 eV (C_2H_2), and −1.03 eV (C_2H_4), demonstrate a clear transition from physisorption (H_2) to chemisorption (C_2H_2 and C_2H_4).

A further examination of CDD in the Pd@$MoSe_2$-WSe_2/gas systems reveals distinct electronic redistribution patterns that elucidate the adsorption mechanisms. On one hand, the pronounced electron accumulation is observed at the newly formed Pd-H and Pd-C bonds, as well as the adsorbed gas molecules, demonstrating substantial charge localization during bond formation and the electron-accepting character of all three gas species [58] that may be attributed to the favorable electron-donating property of the Pd dopant here. On the other hand, significant electron depletion in the H-H bond of the adsorbed H_2 molecule and the C≡C/C=C bonds of C_2H_2/C_2H_4 molecules are correlated with their weakened structural integrity post-adsorption, as evidenced by the discussed bond elongation and molecular distortion. Moreover, quantitative Hirshfeld charge analysis confirms the charge transfer observations, revealing the Q_T values of −0.074, −0.192, and −0.103 e for H_2, C_2H_2, and C_2H_4 systems, respectively. These values not only verify the electron-donating nature of the Pd-doped heterojunction but also exhibit a consistent trend of the Q_T with the calculated E_{ad}, following the order $C_2H_4 > C_2H_2 > H_2$. This consistency between two critical adsorption parameters provides compelling evidence to uncover the relationship between the electronic property and adsorption performance in these gas–surface interactions.

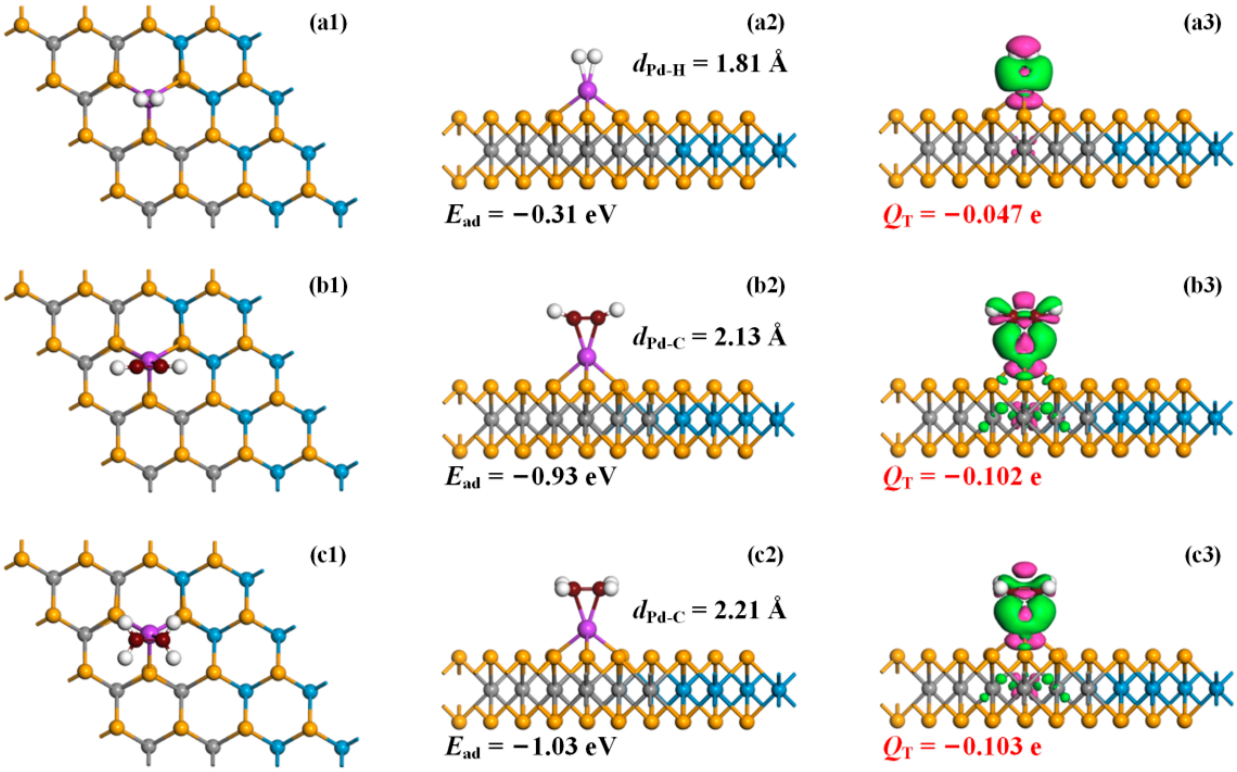


Figure 4. MSC and CDD for gas adsorption on Pd@$MoSe_2$-WSe_2 surface. (**a1**–**a3**) H_2 system, (**b1**–**b3**) C_2H_2 system, and (**c1**–**c3**) C_2H_4 system. In CDD, the sets are the same as Figure 2.

Secondly, our analysis extends to examining the adsorption performance of Pd-$MoSe_2$ and Pd-WSe_2 monolayers for three target gas species (H_2, C_2H_2, and C_2H_4), with Figure 5 displaying their MSC and corresponding CDD plots. It is found that the adsorption geometries across both monolayers appear quite similar, featuring comparable bond lengths of 1.82 Å for Pd-H in the H_2 system, 2.14 Å for Pd-C in the C_2H_2 system, and 2.22 Å for Pd-C in the C_2H_4 system. On the other hand, the thermodynamic and electronic properties reveal significant differences in adsorption strength. The calculated E_{ad} demonstrates systematically stronger interactions for Pd-WSe_2 (−0.18 eV, −0.79 eV, and −0.91 eV for H_2, C_2H_2, and C_2H_4 respectively) compared to Pd-$MoSe_2$ (−0.13 eV, −0.77 eV, and −0.87 eV), a trend corroborated by the Hirshfeld charge analysis showing greater Q_T in Pd-WSe_2/gas systems (−0.039 e, −0.082 e, and −0.090 e) versus Pd-$MoSe_2$/gas systems (−0.032 e, −0.079 e, and −0.084 e).

In short, the above analyses establish a clear hierarchy in gas adsorption performance among three surfaces, Pd@$MoSe_2$-WSe_2 > Pd-WSe_2 > Pd-$MoSe_2$, with the heterojunction structure exhibiting a superior gas capture capability. Notably, the relative adsorption strength of all three substrates upon three gas molecules remains consistent, namely C_2H_4 > C_2H_2 > H_2, with all molecules behaving with an electron-accepting property across all the interactions. These findings suggest that the intrinsic electronic properties of the gas molecules (H_2, C_2H_2, and C_2H_4) can significantly govern their interaction mechanisms with Pd-doped surfaces. However, the substrate composition plays a critical modulating role in determining the ultimate adsorption strength. The observed systematic variations in E_{ad} and Q_T values across different substrates, despite similar adsorption geometries, points to subtle but crucial differences in the interfacial electronic structure and further sensing performances, which will be uncovered through detailed electronic structure analysis.

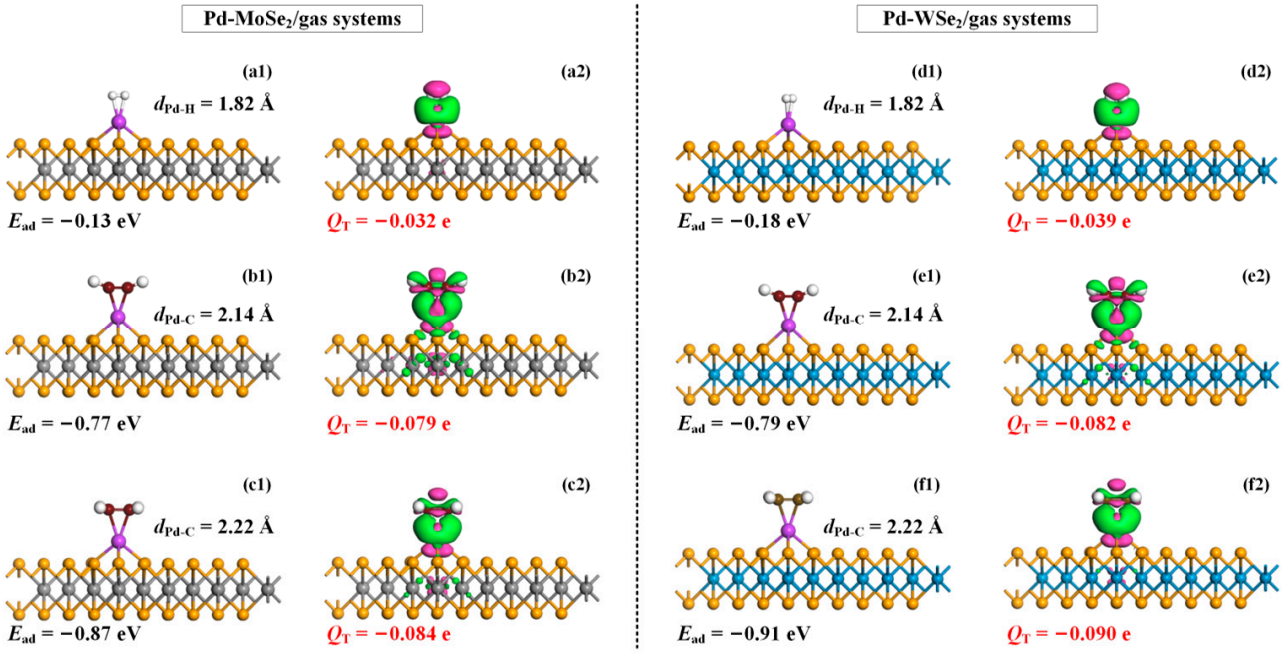


Figure 5. MSC and CDD for gas-adsorbed Pd-$MoSe_2$ and Pd-WSe_2 systems. (**a1**,**a2**) Pd-$MoSe_2$/H_2, (**b1**,**b2**) Pd-$MoSe_2$/C_2H_2, (**c1**,**c2**) Pd-$MoSe_2$/C_2H_4, (**d1**,**d2**) Pd-WSe_2/H_2, (**e1**,**e2**) Pd-WSe_2/C_2H_2, and (**f1**,**f2**) Pd-WSe_2/C_2H_4. In CDD, the sets are the same as Figure 2.

3.3. Analysis of Electronic Property in Gas Adsorption

The above investigation reveals that the Pd@$MoSe_2$-WSe_2 heterojunction exhibits superior gas adsorption characteristics, as evidenced by its exceptional adsorption strength and substantial charge transfer capacity. To elucidate the fundamental mechanisms underlying such a performance, we conduct a detailed analysis of electronic structure modifications by BS and DOS calculations, as plotted in Figure 6. The symmetric spin-up and spin-down states in the BS diagrams confirm that Pd@$MoSe_2$-WSe_2 maintains its non-magnetic character upon gas adsorption, which allows us to focus our analysis on the total DOS rather than separate spin-resolved components.

The BS analysis in the Pd@$MoSe_2$-WSe_2 system upon gas adsorption reveals significant modifications to its electronic properties. Following the adsorption of H_2, C_2H_2, and C_2H_4, the bandgap undergoes progressive narrowing from its initial value of 1.398 eV (isolated system) to 1.321 eV (H_2 system), 1.233 eV (C_2H_2 system), and 1.220 eV (C_2H_4 system), respectively. This bandgap reduction directly translates to enhanced electrical conductivity—a crucial characteristic for resistive gas sensor exploration, as the decreased bandgap facilitates greater charge carrier mobility under operational conditions [59]. Remarkably, despite these electronic modifications, the direct semiconducting nature of the Pd@$MoSe_2$-WSe_2 remains intact across all gas adsorption systems. In addition, the systematic reduction in the bandgap can be attributed to the formation of new interfacial states near the Fermi level through hybridization between gas molecular orbitals and the Pd-doped heterojunction states [60]. This can be illustrated by the total DOS diagrams, where the adsorbed gas molecules introduce additional electronic states that significantly contribute to the overall DOS profile, particularly in the vicinity of the Fermi level. These newly formed states effectively populate the original bandgap region of the isolated system, thereby reducing the effective bandgap and modifying the electronic transport properties [61]. Furthermore, a systematic right-shift in the total DOS is observed in all gas-adsorbed systems compared to the isolated heterojunction, reflecting a reduction in electron density in the conduction band and an increase in hole density in the valence band, both of which are

direct consequences of the charge transfer during adsorption. These observations are in excellent agreement with the Hirshfeld charge analysis results, which demonstrate that the adsorbed gas molecules accept electrons from the Pd-doped heterojunction.

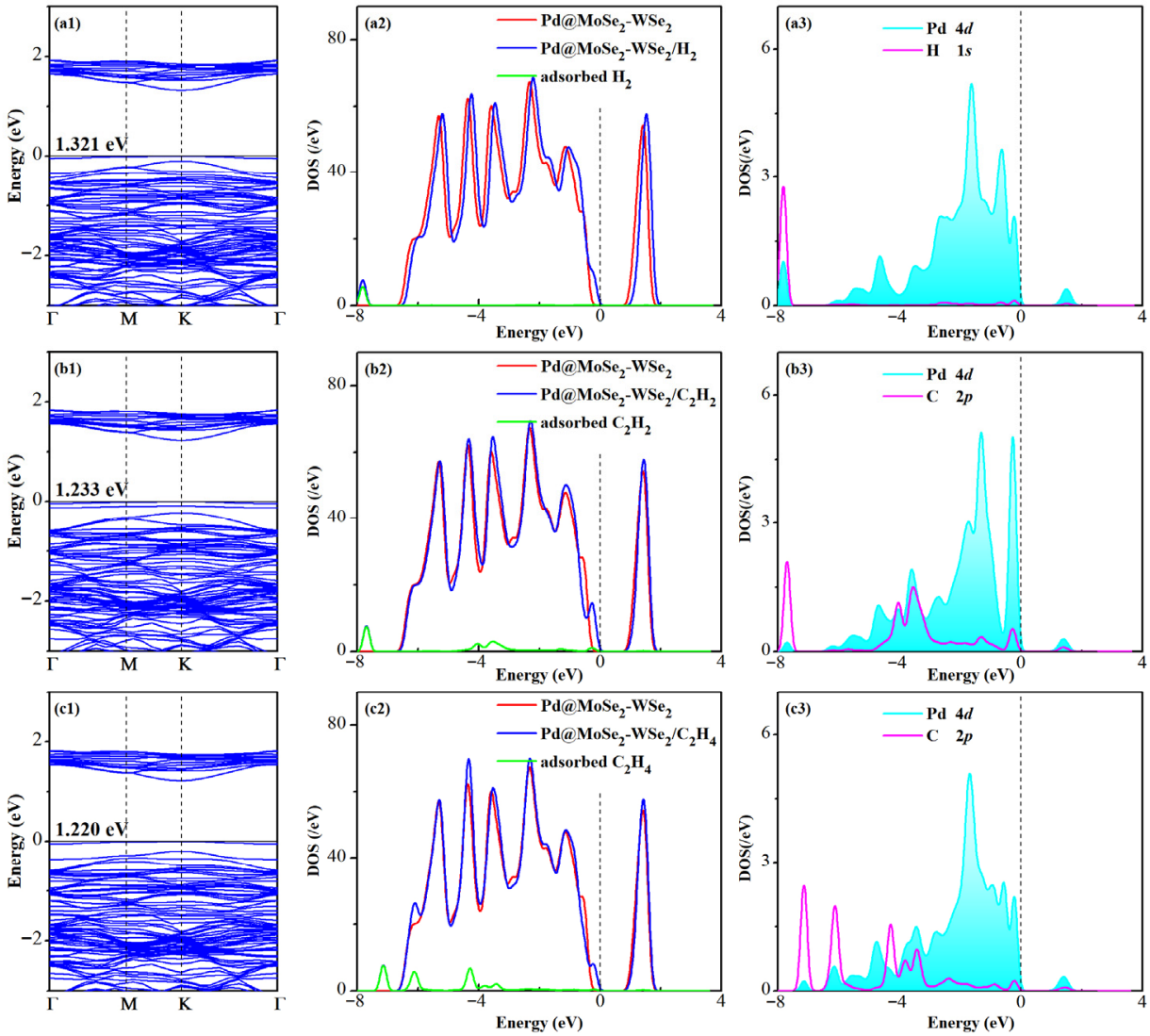


Figure 6. BS and DOS of gas-adsorbed Pd@$MoSe_2$-WSe_2 systems. (**a1**– **a3**) H_2 system, (**b1**–**b3**) C_2H_2 system, and (**c1**–**c3**) C_2H_4 system. The sets are the same as Figure 3.

A further orbital DOS analysis can provide atomic-level insights into the nature of gas–surface interactions in the Pd@$MoSe_2$-WSe_2 system, revealing distinct hybridization patterns that explain the observed adsorption behavior. For the H_2 adsorption system, the DOS shows minimal overlap between Pd 4*d* and H 1*s* orbitals, with weak hybridization features appearing deep below the Fermi level (around −8 eV). This is consistent with the relatively weak physisorption character indicated by the modest adsorption energy (−0.31 eV). In striking contrast, the C_2H_2 and C_2H_4 adsorption systems exhibit pronounced orbital hybridization between Pd 4*d* and C 2*p* states near the Fermi level. This interfacial orbital interaction correlates with the much stronger adsorption strength observed for these systems (−0.93 eV for C_2H_2 and −1.03 eV for C_2H_4). The spatial distribution of these hybrid states shows substantial electron density overlap between Pd and C atoms, providing direct electronic evidence for the formation of stable Pd-C chemical bonds [62].

Subsequently, our investigation focuses on the electronic bandgap modifications on Pd-$MoSe_2$ and Pd-WSe_2 monolayers, with the BS diagrams exhibited in Figure 7. The comparative analysis demonstrates that both monolayers undergo characteristic bandgap reductions upon gas adsorption, though with distinct magnitudes reflecting their different electronic properties. For the Pd-$MoSe_2$ system, adsorption induces bandgap narrowing from 1.422 eV (isolated) to 1.391 eV (H_2), 1.286 eV (C_2H_2), and 1.321 eV (C_2H_4), while the Pd-WSe_2 system shows reductions from 1.464 eV (isolated) to 1.403 eV (H_2), 1.312 eV (C_2H_2), and 1.304 eV (C_2H_4). These bandgap changes in two monolayer/gas systems are consistent and correlate well with the previous hierarchy of E_{ad} and Q_T ($C_2H_4 > C_2H_2 > H_2$). The observed electronic deformations originate from gas-induced states within the original bandgap, with the extent of bandgap narrowing directly reflecting the strength of orbital hybridization between adsorbate molecules and the Pd dopant. Importantly, these tunable electronic properties establish the fundamental working principle for resistive gas sensing, where bandgap-mediated conductivity changes serve as the primary detection mechanism [63]. These comparative evaluations of sensing performance across three Pd-doped systems (Pd@$MoSe_2$-WSe_2, Pd-WSe_2, and Pd-$MoSe_2$) can provide a complete illustration of structure–property relationships in these sensing materials, which will be analyzed in the next section.

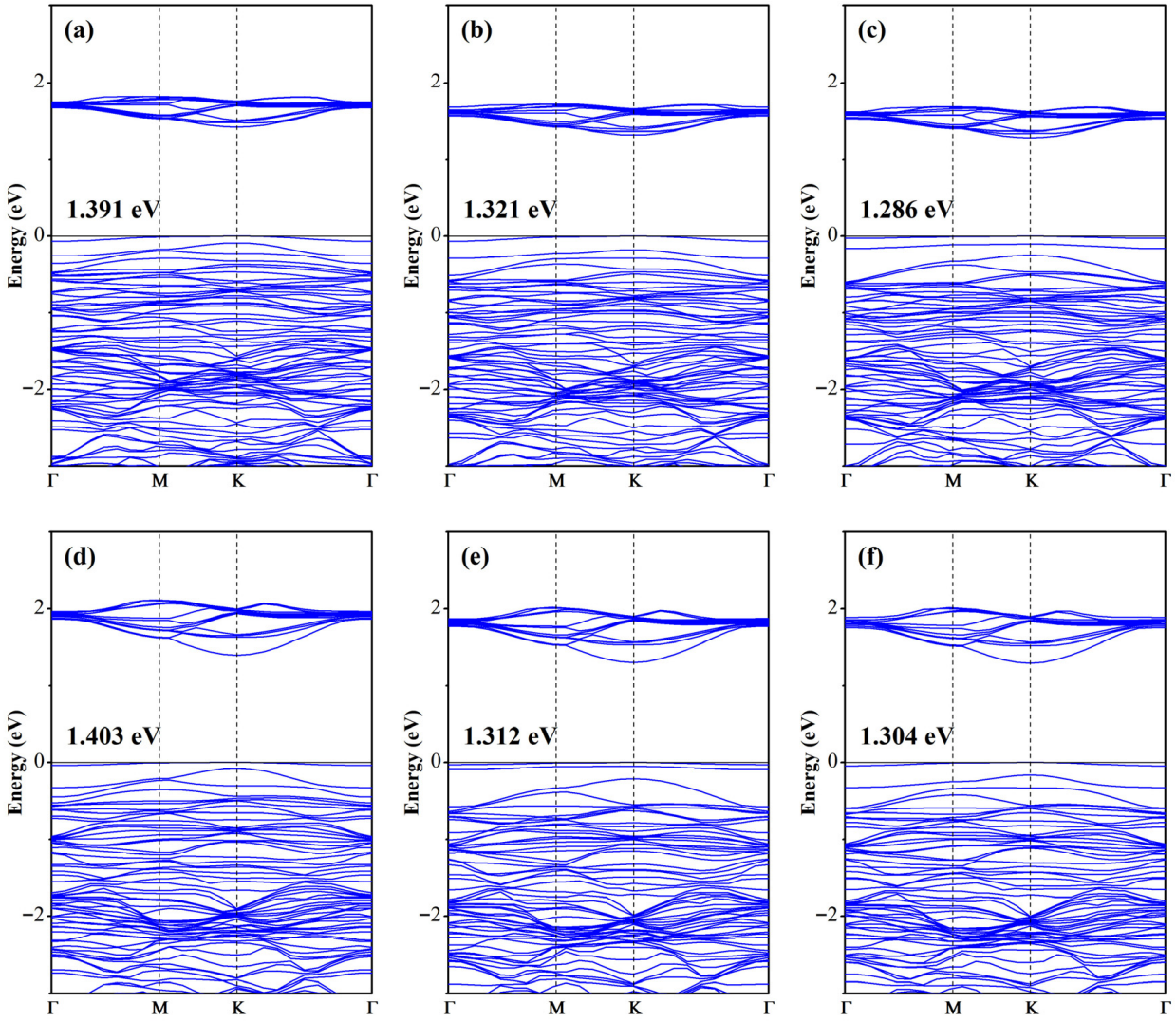


Figure 7. BS of gas-adsorbed Pd-$MoSe_2$ and Pd-WSe_2 systems. (**a**) Pd-$MoSe_2$/H_2, (**b**) Pd-$MoSe_2$/C_2H_2, (**c**) Pd-$MoSe_2$/C_2H_4, (**d**) Pd-WSe_2/H_2, (**e**) Pd-WSe_2/C_2H_2, and (**f**) Pd-WSe_2/C_2H_4. The black values are bandgaps.

3.4. Gas Sensor Exploration

Building upon the established correlation between the bandgap reduction and enhanced electrical conductivity in three Pd-doped systems, we herein present a theoretical framework to evaluate their resistive gas sensing potentials and performances. The fundamental relationship governing the electrical conductivity (σ) of these nanomaterials by their bandgap (B_g) follows the Arrhenius-type expression, expressed as [25]

$$\sigma = \lambda \cdot e^{(-B_g/2kT)} \tag{6}$$

where λ represents a constant, T is the operating temperature (typically room temperature, 298 K), and k denotes the Boltzmann constant (1.38×10^{-23} J/K) [64].

This formula originates from the intrinsic carrier concentration n, which is proportional to the probability of thermal excitation across the bandgap. Although, in the DMol^3 module, the Fermi level in the BS plot is typically set to align with the highest occupied state (the valence band maximum) by default for visualization clarity. However, this does not represent the true electrochemical potential of the system in its charge-neutral ground state. For a semiconductor where the Fermi level lies near the mid-gap, the activation energy for this process is $B_g/2$. For the semiconductors of three Pd-doped systems in this work, the Fermi level must lie close to the middle of the bandgap. Therefore, using $B_g/2$ is based on the physical definition of the Fermi level in a semiconductor rather than its default position in the specific computational output. The factor λ encompasses the carrier mobility and other kinetic parameters, which are assumed to have a weaker, often power-law dependence on temperature compared to the dominant exponential factor. This model is valid in the intrinsic conduction regime where thermal generation of electron–hole pairs is the primary conduction mechanism. More critically, the sensing response (S), which quantifies the relative change in electrical resistance upon gas exposure, can be derived through the following equation [65]:

$$S = ({\sigma_{\text{gas}}}^{-1} - {\sigma_{\text{isolated}}}^{-1})/{\sigma_{\text{isolated}}}^{-1} \tag{7}$$

where σ_{gas} and $\sigma_{isolated}$ represent the conductivity of the gas-adsorbed and isolated systems, respectively. By combining these relationships, we arrive at Equation (8), which directly correlates the S with the bandgap reduction (ΔB_g) induced by gas adsorption.

$$S = \mathrm{e}^{\Delta B_g/2kT} - 1 \tag{8}$$

For better observation, we list the bandgap of three Pd-doped systems as well as their gas-adsorbed system in Table 1, with the calculated S upon H_2, C_2H_2, and C_2H_4 at room temperature (298 K) displayed in Figure 8.

Table 1. Bandgaps of isolated and gas-adsorbed Pd@$MoSe_2$-WSe_2, Pd-$MoSe_2$, and Pd-WSe_2 monolayers.

Gas Species	Bandgaps of Various Systems (eV)		
	Pd@$MoSe_2$-WSe_2	**Pd-$MoSe_2$**	**Pd-WSe_2**
Isolated	1.398	1.422	1.464
H_2	1.321	1.391	1.403
C_2H_2	1.233	1.321	1.312
C_2H_4	1.220	1.286	1.304

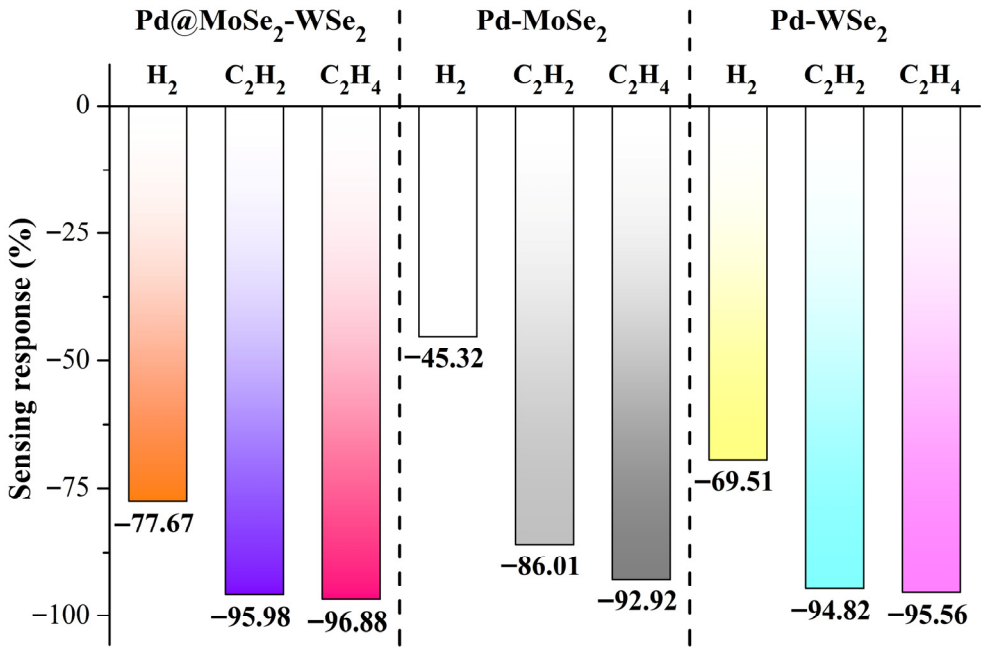


Figure 8. Sensing responses of three Pd-doped monolayers upon H_2, C_2H_2 and C_2H_4 at room temperature.

The calculated *S* values reveal the remarkable gas detection performance of the Pd@$MoSe_2$-WSe_2 heterojunction, with favorable negative responses of −77.67% (H_2), −95.98% (C_2H_2), and −96.88% (C_2H_4). These substantial response magnitudes, particularly for C_2H_2 and C_2H_4 detection, imply the heterojunction's superior sensitivity that stems from its notable interfacial characteristics. The observed response hierarchy (C_2H_4 > C_2H_2 > H_2) directly correlates with the degree of E_{ad} and Q_T, manifesting that the stronger interactions induce more significant electronic structure perturbations and consequently larger conductivity changes [66]. Moreover, the comparative analysis of *S* with Pd-$MoSe_2$ (−45.32%, −86.01%, and −92.92%) and Pd-WSe_2 (−69.51%, −94.82%, and −95.96%) monolayers upon H_2, C_2H_2, and C_2H_4 further demonstrates the better sensing performance of the heterojunction than the isolated monolayer, with the Pd@$MoSe_2$-WSe_2 system exhibiting a 1.7–2.4 times greater response for H_2 and consistently superior performance for hydrocarbon gases. This enhanced sensing capability originates from the unique property of the heterojunction compared with the isolated monolayers, which is a combination of multiple enhancement mechanisms operating at the atomic scale. Firstly, the built-in potential at the heterojunction interface creates an intrinsic electric field that significantly facilitates electron mobility and charge transfer processes, thereby amplifying the overall charge transfer (Q_T) with the gas molecules [67]. Concurrently, the induced interfacial strain generates localized structural distortions that not only increase the density of available active sites but also modify their electronic environment, thus promoting the adsorption behavior with a larger E_{ad} [68]. Additionally, the Pd dopant at the heterojunction interface further modifies the local electronic structure, with the combined catalytic effect creating additional active sites for gas adsorption [69]. These modifications collectively lower the activation energy for gas–surface interactions while increasing the density of states near the Fermi level, resulting in accelerated reaction kinetics and substantially improved gas response characteristics.

In short, these findings not only position Pd@$MoSe_2$-WSe_2 as an outstanding candidate for DGA in oil-filled transformers but also establish a structure–property relationship that uncovers the feasibility of a strategic heterojunction design to enhance the adsorption

and sensing performances for typical gas species. Such performance metrics meet and even exceed the requirements for the current transformer monitoring systems, offering a promising solution for early fault detection and prevention in power grid applications.

4. Conclusions

This study presents a comprehensive first-principles investigation into the gas adsorption and sensing performances of Pd-$MoSe_2$, Pd-WSe_2, and Pd@$MoSe_2$-WSe_2 systems for DGA in oil-filled transformers. A Pd atom is integrated onto the $MoSe_2$, WSe_2, and $MoSe_2$-WSe_2 surface to establish the Pd-doped systems, with an E_{coh1}, E_{coh2}, and E_{coh3} of −1.88, −3.20, and −3.06 eV, respectively. The analysis of adsorption configurations and parameters reveals a consistent hierarchy in gas adsorption strength across all three systems, with binding affinity following the order of C_2H_4 > C_2H_2 > H_2 and substrate performance ranks as Pd@$MoSe_2$-WSe_2 > Pd-WSe_2 > Pd-$MoSe_2$. Then, the analysis of the electronic structure shows pronounced bandgap modifications upon gas adsorption, correlating with the exceptional sensing responses observed in Pd@$MoSe_2$-WSe_2 (−77.67% for H_2, −95.98% for C_2H_2, and −96.88% for C_2H_4), which exceed those of the monolayer counterparts underscoring the critical role of heterojunction engineering in optimizing the gas sensing performance. Such a performance, with an analyzed mechanism for enhancement in the sensing response, positions Pd@$MoSe_2$-WSe_2 as a promising material for DGA in oil-filled transformers. Furthermore, this work establishes a fundamental design for developing advanced TMD heterostructures with tailored sensitivity profiles, offering opportunities for early fault detection and predictive maintenance in power grid systems.

Author Contributions: Formal analysis, S.M.; Investigation, S.M.; Writing – original draft, X.G.; Writing – review & editing, H.C.; Supervision, H.C.; Funding acquisition, H.C. All authors have read and agreed to the published version of the manuscript.

Funding: This work is funded by National Natural Science Foundation of China (No. 52207175).

Institutional Review Board Statement: Not applicable.

Informed Consent Statement: Not applicable.

Data Availability Statement: The data presented in this study are available on request from the corresponding author.

Acknowledgments: The authors acknowledge the use of the high-performance workstation (Dual Intel Xeon E5-2678 v3 CPUs, 24 cores @ 2.50 GHz, 128 GB RAM) for completing the computational simulations in this work.

Conflicts of Interest: Authors Xinyu Guo and Shouxiao Ma were employed by the company CHN Energy Qinghai Electric Power Co., Ltd . The remaining authors declare that the research was conducted in the absence of any commercial or financial relationships that could be construed as a potential conflict of interest.

References

1. Cui, H.; Chen, D.; Zhang, Y.; Zhang, X. Dissolved gas analysis in transformer oil using Pd catalyst decorated MoSe2 monolayer: A first-principles theory. *Sustain. Mater. Technol.* **2019**, *20*, e00094. [CrossRef]
2. Zhou, Q.; Zhang, G.; Tian, S.; Zhang, X. First-Principles Insight into Pd-Doped ZnO Monolayers as a Promising Scavenger for Dissolved Gas Analysis in Transformer Oil. *ACS Omega* **2020**, *5*, 17801–17807. [CrossRef]
3. Baek, D.H.; Kim, J. MoS_2 gas sensor functionalized by Pd for the detection of hydrogen. *Sens. Actuators B Chem.* **2017**, *250*, 686–691. [CrossRef]
4. Lu, Y.C.; Wei, L.; Chao, W.; Peng, W. The New Development Trend of Distribution Transformer. *Appl. Mech. Mater.* **2014**, *672–674*, 831–836. [CrossRef]
5. Liao, R.; Zheng, H.; Grzybowski, S.; Yang, L.; Zhang, Y.; Liao, Y. An Integrated Decision-Making Model for Condition Assessment of Power Transformers Using Fuzzy Approach and Evidential Reasoning. *IEEE Trans. Power Deliv.* **2011**, *26*, 1111–1118. [CrossRef]

6. Singh, S.; Bandyopadhyay, M.N. Dissolved gas analysis technique for incipient fault diagnosis in power transformers: A bibliographic survey. *IEEE Electr. Insul. Mag.* **2010**, *26*, 41–46. [CrossRef]
7. He, X.; Gui, Y.; Xie, J.; Liu, X.; Wang, Q.; Tang, C. A DFT study of dissolved gas (C_2H_2, H_2, CH_4) detection in oil on CuO-modified BNNT. *Appl. Surf. Sci.* **2020**, *500*, 144030. [CrossRef]
8. Yang, F.; Jung, D.; Penner, R.M. Trace Detection of Dissolved Hydrogen Gas in Oil Using a Palladium Nanowire Array. *Anal. Chem.* **2011**, *83*, 9472–9477. [CrossRef]
9. Ding, J.; Li, X.; Cao, J.; Sheng, L.; Yin, L.; Xu, X. New sensor for gases dissolved in transformer oil based on solid oxide fuel cell. *Sens. Actuators B Chem.* **2014**, *202*, 232–239. [CrossRef]
10. Ma, G.M.; Li, C.R.; Luo, Y.T.; Mu, R.D.; Wang, L. High sensitive and reliable fiber Bragg grating hydrogen sensor for fault detection of power transformer. *Sens. Actuators B Chem.* **2012**, *169*, 195–198. [CrossRef]
11. Benounis, M.; Aka-Ngnui, T.; Jaffrezic, N.; Dutasta, J.P. NIR and optical fiber sensor for gases detection produced by transformation oil degradation. *Sens. Actuators A Phys.* **2008**, *141*, 76–83. [CrossRef]
12. Zhang, G.; Zhang, X.; Cheng, H.; Tang, J. Ladder-wise calculation method for z-coordinate of transformer PD source based on planar layout UHF antenna sensors. *IEEJ Trans. Electr. Electron. Eng.* **2019**, *15*, 340–345. [CrossRef]
13. Cui, H.; Zhang, G.; Zhang, X.; Tang, J. Rh-doped $MoSe_2$ as toxic gas scavenger: A first-principles study. *Nanoscale Adv.* **2019**, *2019*, 772–780. [CrossRef] [PubMed]
14. Cui, H.; Zhang, X.; Zhang, J.; Zhang, Y. Nanomaterials-based gas sensors of SF6 decomposed species for evaluating the operation status of high-voltage insulation devices. *High Volt.* **2019**, *4*, 242–258. [CrossRef]
15. Sajjad, M.; Montes, E.; Singh, N.; Schwingenschlögl, U. Superior Gas Sensing Properties of Monolayer PtSe2. *Adv. Mater. Interfaces* **2017**, *4*, 1600911. [CrossRef]
16. Yang, H.; Wang, Z.; Ye, H.; Zhang, K.; Chen, X.; Zhang, G. Promoting sensitivity and selectivity of HCHO sensor based on strained InP3 monolayer: A DFT study. *Appl. Surf. Sci.* **2018**, *459*, 554–561. [CrossRef]
17. Cui, H.; Ran, M.; Peng, X.; Zhang, G. First-principles design of noble metal (Rh and Pd) dispersed Janus WSTe monolayer for toxic gas sensing applications. *J. Environ. Chem. Eng.* **2024**, *12*, 112047. [CrossRef]
18. Zhang, D.; Yang, Z.; Li, P.; Pang, M.; Xue, Q. Flexible self-powered high-performance ammonia sensor based on Au-decorated MoSe2 nanoflowers driven by single layer MoS2-flake piezoelectric nanogenerator. *Nano Energy* **2019**, *65*, 103974. [CrossRef]
19. Shokri, A.; Salami, N. Gas sensor based on MoS2 monolayer. *Sens. Actuators B Chem.* **2016**, *236*, 378–385. [CrossRef]
20. Lin, Y.F.; Xu, Y.; Wang, S.T.; Li, S.L.; Yamamoto, M.; Aparecido-Ferreira, A.; Li, W.; Sun, H.; Shu, N.; Jian, W.B. Ambipolar MoTe2 Transistors and Their Applications in Logic Circuits. *Adv. Mater.* **2014**, *26*, 3263–3269. [CrossRef]
21. Cui, H.; Zhang, X.; Zhang, G.; Tang, J. Pd-doped MoS2 monolayer: A promising candidate for DGA in transformer oil based on DFT method. *Appl. Surf. Sci.* **2019**, *470*, 1035–1042. [CrossRef]
22. Wu, E.; Xie, Y.; Yuan, B.; Zhang, H.; Hu, X.; Liu, J.; Zhang, D. Ultra-sensitive and Fully Reversible NO_2 Gas Sensing based on p-type MoTe2 Under ultra-violet Illumination. *ACS Sens.* **2018**, *3*, 1719–1726.
23. Zhang, Y.; Yang, R.; Li, H.; Zeng, Z. Boosting Electrocatalytic Reduction of CO_2 to HCOOH on Ni Single Atom Anchored WTe2 Monolayer. *Small* **2022**, *18*, 2203759. [CrossRef]
24. Xu, L.; Gui, Y.; Li, W.; Li, Q.; Chen, X. Gas-sensing properties of Ptn-doped WSe2 to SF6 decomposition products. *J. Ind. Eng. Chem.* **2021**, *97*, 452–459. [CrossRef]
25. Cui, H.; Wu, H.; He, D.; Ma, S. Noble metal (Pd, Pt)-functionalized WSe2 monolayer for adsorbing and sensing thermal runaway gases in LIBs: A first-principles investigation. *Environ. Res.* **2025**, *269*, 120847. [CrossRef] [PubMed]
26. Zhang, X.; Yu, L.; Wu, X.; Hu, W. Experimental Sensing and Density Functional Theory Study of H2S and SOF2 Adsorption on Au-Modified Graphene. *Adv. Sci.* **2015**, *2*, 612.
27. Zhang, X.; Yu, L.; Gui, Y.; Hu, W. First-principles study of SF6 decomposed gas adsorbed on Au-decorated graphene. *Appl. Surf. Sci.* **2016**, *367*, 259–269. [CrossRef]
28. Wang, G.; Yuan, H.; Chang, J.; Wang, B.; Kuang, A.; Chen, H. ZnO/MoX 2 (X= S, Se) composites used for visible light photocatalysis. *RSC Adv.* **2018**, *8*, 10828–10835. [CrossRef] [PubMed]
29. Zhang, D.; Yu, S.; Wang, X.; Huang, J.; Pan, W.; Zhang, J.; Meteku, B.E.; Zeng, J. UV illumination-enhanced ultrasensitive ammonia gas sensor based on (001) TiO_2/MXene heterostructure for food spoilage detection. *J. Hazard. Mater.* **2022**, *423*, 127160. [CrossRef]
30. Ikram, M.; Liu, L.; Liu, Y.; Ma, L.; Lv, H.; Ullah, M.; He, L.; Wu, H.; Wang, R.; Shi, K. Fabrication and characterization of a high-surface area MoS2@ WS2 heterojunction for the ultra-sensitive NO_2 detection at room temperature. *J. Mater. Chem. A* **2019**, *7*, 14602–14612. [CrossRef]
31. Kalita, P.; Sutradhar, M.K.; Mondal, B. Hybrid MoSe2/WSe2 Nanomaterials: Enhancing Humidity Tolerant Gas Response. *IEEE Sens. Lett.* **2023**, *7*, 1–4. [CrossRef]
32. Creazzo, F. Engineering of MoSe2 and WSe2 Monolayers and Heterostructures by DFT-Molecular Dynamics Simulations. *ACS Appl. Mater. Interfaces* **2025**, *17*, 39676–39693. [CrossRef]

33. Li, Z.; Liao, Y.; Liu, Y.; Zeng, W.; Zhou, Q. Room temperature detection of nitrogen dioxide gas sensor based on Pt-modified MoSe2 nanoflowers: Experimental and theoretical analysis. *Appl. Surf. Sci.* **2023**, *610*, 155527. [CrossRef]
34. Tan, X.; Zhou, F. Detection of Dissolved Gas in Transformer Oil Using Pt-Doped WTe 2 Based Sensor: A First Principles Study. In Proceedings of the 2023 IEEE 6th International Electrical and Energy Conference (CIEEC), Hefei, China, 12–14 May 2023; pp. 733–736.
35. Ding, H.; Qin, Z.; Sun, X.; Wang, B.; Wang, F. Pd-Adsorbing CrS2 monolayer as sensing material for detecting CO, C2H2, and C2H4 in dissolved gases: A first-principles study. *Chem. Phys. Lett.* **2024**, *857*, 141700. [CrossRef]
36. Cui, H.; Guo, Y.; Zhao, Q.; Zhang, G. Pd-doped PtSe2 monolayer with strain-modulated effect for sensing SF6 decomposed species: A first-principles study. *J. Mater. Res. Technol.* **2022**, *18*, 629–636. [CrossRef]
37. Chen, D.; Zhang, X.; Xiong, H.; Li, Y.; Zhang, D. A first-principles study of the SF6 decomposed products adsorbed over defective WS2 monolayer as promising gas sensing device. *IEEE Trans. Device Mater. Reliab.* **2019**, *19*, 473–483. [CrossRef]
38. Cui, H.; Jia, P.; Peng, X. Adsorption of SO_2 and NO_2 molecule on intrinsic and Pd-doped HfSe2 monolayer: A first-principles study. *Appl. Surf. Sci.* **2020**, *513*, 145863. [CrossRef]
39. Tkatchenko, A.; Di Stasio, R.A., Jr.; Head-Gordon, M.; Scheffler, M. Dispersion-corrected Møller-Plesset second-order perturbation theory. *J. Chem. Phys.* **2009**, *131*, 094106. [CrossRef]
40. Yang, A.; Pan, J.; Wang, D.; Lan, T.; Liu, Z.; Yuan, H.; Chu, J.; Wang, X.; Rong, M. Tunable SO_2-sensing performance of arsenene induced by Stone-Wales defects and external electric field. *Appl. Surf. Sci.* **2020**, *523*, 146403. [CrossRef]
41. Cui, H.; Yan, C.; Jia, P.; Cao, W. Adsorption and sensing behaviors of SF6 decomposed species on Ni-doped C3N monolayer: A first-principles study. *Appl. Surf. Sci.* **2020**, *512*, 145759. [CrossRef]
42. Cui, H.; Hu, J.; Jiang, X.; Zhang, X. A first-principles study of SOF2 and SO2F2 adsorption onto PdSe2-based monolayers: Favorable sensitivity and selectivity by doping single Cu or Rh atom. *Environ. Res.* **2025**, *269*, 120843. [CrossRef] [PubMed]
43. Ma, D.; Zeng, Z.; Liu, L.; Jia, Y. Theoretical screening of the transition metal heteronuclear dimer anchored graphdiyne for electrocatalytic nitrogen reduction. *J. Energy Chem.* **2021**, *54*, 501–509. [CrossRef]
44. Wu, H.; Fang, J.; Yuan, S.; Liu, Y.; Zeng, J.; Jiang, T. Adsorption and gas sensing properties of Cun and Pdn (n = 1–3) clusters modified MoSe2 for lithium battery thermal runaway gases. *Appl. Surf. Sci.* **2024**, *648*, 158963. [CrossRef]
45. Zhang, H.; Huang, Z.; Jiang, J.; Zeng, W.; Zhou, Q. DFT study of Cun (n = 1–3) cluster-modified WSe2 monolayers for the detection of SF6 decomposition gases (H2S, SO2, SOF2 and SO2F2). *Surf. Interfaces* **2024**, *52*, 104904. [CrossRef]
46. Pyykkö, P.; Atsumi, M. Molecular single-bond covalent radii for elements 1-118. *Chemistry* **2009**, *15*, 186–197. [CrossRef]
47. Tang, M.; Zhang, D.; Wang, D.; Deng, J.; Kong, D.; Zhang, H. Performance prediction of 2D vertically stacked MoS2-WS2 heterostructures base on first-principles theory and Pearson correlation coefficient. *Appl. Surf. Sci.* **2022**, *596*, 153498. [CrossRef]
48. Xue, S.; Huang, Z.; Yun, M.; Liu, D.; Pan, Z.; Yang, D. The adsorption characteristics of MoS_2–CuO heterojunction to polar gas molecules (CO, NO and NO2): A first–principle study. *Appl. Surf. Sci.* **2023**, *610*, 155564. [CrossRef]
49. Zhang, M.; Zhang, J. Highly Selective NH3 Sensor Based on MoS_2/WS2 Heterojunction. *Nanomaterials* **2023**, *13*, 1835. [CrossRef] [PubMed]
50. Zheng, W.; Lu, G.; Liu, X.; Fan, S.; Hu, Y.; Pinna, N.; Zhang, J. Mixed-dimensional heterojunction by 3D CdS nanowire arrays bridged with 2D WSe2 for ultrafast photoelectric gas sensor. *Matter* **2024**, *8*, 101914. [CrossRef]
51. Zhai, S.; Jiang, X.; Wu, D.; Chen, L.; Su, Y.; Cui, H.; Wu, F. Single Rh atom decorated pristine and S-defected PdS2 monolayer for sensing thermal runaway gases in a lithium-ion battery: A first-principles study. *Surf. Interfaces* **2023**, *37*, 102735. [CrossRef]
52. Gao, J.; Gao, K.; Miao, L.; Ding, J.; Chen, H.; Fu, H.; Peng, J. First principle investigation on gas sensing properties of MoS_2/ZnO heterojunction. *Microchem. J.* **2024**, *206*, 111414. [CrossRef]
53. Murphy, L.R.; Meek, T.L.; Allred, A.L.; Allen, L.C. Evaluation and test of pauling's electronegativity scale. *J. Phys. Chem. A* **2000**, *104*, 5867–5871. [CrossRef]
54. Xingyi, T.; Qiang, L.; Hua-Hua, D.F. The device performance limit of in-plane monolayer VTe2/WTe2 heterojunction-based field-effect transistors. *Nanoscale* **2023**, *15*, 19726–19734.
55. Li, F.; Chen, F.; Cui, H.; Jiang, X. Pristine and Ni-doped WTe2 monolayer for adsorption and sensing of C_2H_2 and C_2H_4 in oil-immersed transformers: A DFT study. *Comput. Theor. Chem.* **2023**, *1226*, 114187. [CrossRef]
56. Tang, M.; Zhang, D.; Chen, Q.; Wang, Z.; Wang, D.; Yang, Z.; Xu, W.; Wang, L.; Zhu, L.; An, F. Heterostructure construction of SnS2 Debye nanowires modified with ZnO nanorods for chemiresistive H2S detection in sulfur hexafluoride decomposition products. *Sens. Actuators B Chem.* **2023**, *390*, 133952. [CrossRef]
57. Jiang, T.; Zhang, W.; Zhang, T.; Yuan, H.; Bi, M.; Zhou, X. Adsorption and gas-sensing performances of C_2H_2, C_2H_4, CO, H_2 in transformer oil on Pt-doped MoTe2 monolayer: A DFT study. *Phys. E Low-Dimens. Syst. Nanostruct.* **2022**, *146*, 115568. [CrossRef]
58. Zhang, J.; Wang, Y.; Wei, Z.; Wang, Q.; Liang, Z.; Yuan, T. Ni-Decorated ZnO Monolayer for Sensing CO and HCHO in Dry-Type Transformers: A First-Principles Theory. *Chemosensors* **2022**, *10*, 307. [CrossRef]
59. Liu, Y.; Zhou, Q.; Mi, H.; Wang, J.; Zeng, W. Gas-sensing mechanism of Cr doped SnP3 monolayer to SF6 partial discharge decomposition components. *Appl. Surf. Sci.* **2021**, *546*, 149084. [CrossRef]

60. Reza Khoshnobish, S.; Ahmed, T.; Arefin, T.; Akter Piya, A.; Ud Daula Shamim, S. Assessing the sensing performance of Janus transition metal dichalcogenides (ScSSe, TiSSe and ZrSSe) for oxygen-containing toxic gas molecules such as CO, NO, NO_2 and SO2. *Appl. Surf. Sci.* **2025**, *679*, 161301. [CrossRef]
61. Zhang, D.; Li, Q.; Li, P.; Pang, M.; Luo, Y. Fabrication of Pd-decorated MoSe 2 nanoflowers and density functional theory simulation toward ammonia sensing. *IEEE Electron Device Lett.* **2019**, *40*, 616–619. [CrossRef]
62. Li, J.; Zhang, Y.; Xiong, H.; Deng, G.; Gan, L. Theoretical investigations of adsorption and sensing properties of M2Pc (M= Cr, Mo) monolayers towards volatile organic compounds. *Colloids Surf. A Physicochem. Eng. Asp.* **2025**, *717*, 136750. [CrossRef]
63. He, W.; Xu, Y.; Wu, Z.; Hou, Z.; Qin, W.; Liu, X.; Shi, J.; Long, Y. Adsorption of Nitrogen-Containing Toxic Gases on Transition Metal (Pt, Ag, Au)-Modified Janus ZrSSe Monolayers for Sensing Applications: A DFT Study. *ACS Appl. Nano Mater.* **2025**, *8*, 3163–3174. [CrossRef]
64. Wu, H.; Xia, Y.; Zhang, C.; Xie, S.; Wu, S.; Cui, H. Adsorptions of C5F10O decomposed compounds on the Cu-decorated NiS2 monolayer: A first-principles theory. *Mol. Phys.* **2023**, *121*, e2163715. [CrossRef]
65. Verlag, S. Semiconductor Physical Electronics. *Semicond. Phys. Electron.* **2006**, *28*, 363–364.
66. Liu, L.; Li, Y.; Jiang, X.; Zhang, Z.; Li, T.; Ma, L.; Niu, S.; Chen, Z.; Xiao, S.; Dan, M.; et al. Ir-doped MoSe2: A promising candidate for C4F7N decomposed species detection and scavenging. *Surf. Interfaces* **2024**, *51*, 104634. [CrossRef]
67. Wu, H.; Zhong, S.; Bin, Y.; Jiang, X.; Cui, H. Ni-decorated WS2-WSe2 heterostructure as a novel sensing candidate upon C_2H_2 and C_2H_4 in oil-filled transformers: A first-principles investigation. *Mol. Phys.* **2025**, e2492391. [CrossRef]
68. Li, Z.; Rao, Y.; Wang, Z.; Zhang, T.; Wu, G.; Sun, L.; Ren, Y.; Tao, L. Universal Synthesis of Core–Shell-Structured Ordered Mesoporous Transition Metal Dichalcogenides/Metal Oxides Heterostructures with Active Edge Sites. *Small Struct.* **2025**, *6*, 2400376. [CrossRef]
69. Wang, K.; Fu, Y.; Kong, D.; Wang, S.; Li, L. First-principles insight into adsorption behavior of a Pd-doped PtTe2 monolayer for CO and C2H2 and the effect of an applied electric field. *J. Phys. Chem. Solids* **2023**, *177*, 111289. [CrossRef]

Disclaimer/Publisher's Note: The statements, opinions and data contained in all publications are solely those of the individual author(s) and contributor(s) and not of MDPI and/or the editor(s). MDPI and/or the editor(s) disclaim responsibility for any injury to people or property resulting from any ideas, methods, instructions or products referred to in the content.